Enhancing detectivity in multi-barrier Ag_2Se-PbS CQD photodetector through numerical optimization of design parameters

M. Khodverdizadeh[a] and A. Asgari[b,c,d]

[a] *Optics and Laser Engineering Group, Faculty of Science and Modern Technologies, Urmia University of Technology,*
Urmia 57155-419, Iran.
[b] *Faculty of Physics, University of Tabriz, Tabriz, 51665-163, Iran.*
[c] *Photonics Devices Research Group, Research Institute of Applied Physics and Astronomy,*
University of Tabriz, Tabriz, 51665-163, Iran.
[d] *School of Electrical, Electronic, and Computer Engineering, University of Western Australia,*
Crawley, WA, 6009, Australia.

Received 8 June 2024; accepted 19 February 2025

Colloidal quantum dots (CQDs) with variable narrow bandgaps have emerged as powerful competitors to epitaxially grown semiconductors in the domain of infrared light transitions. This class of materials holds great promise for the development of next-generation optoelectronic devices, especially photodetectors. In recent developments, the use of silver chalcogenide CQDs has expanded to biomedical applications of quantum dots. This expansion is attributed to their advantageous properties, such as low toxicity and tunable intraband transitions reaching the mid-infrared window. In this research, we investigate a structure for mid-infrared photon detection in the form of an intraband Ag_2Se-PbS colloidal quantum dot (CQD) photodetector. Detectivity, a crucial performance parameter, is enhanced through numerical optimization by manipulating key design parameters such as Ag_2Se CQD diameter, Ag_2Se film doping density, and the number of PbS CQD layers in the barrier layer of the device's active region. This optimization process is conducted at various temperatures and biases. The results reveal that, under the conditions of 1 V bias and 80 K , the designed Ag_2Se-PbS CQD infrared photodetector achieves peak detectivities. Specifically, the peak detectivities of 13.13×10^9 Jones for Ag_2Se CQDs with a diameter of 3.7 nm and 11.01×10^9 Jones for a film doping density of 6.7×10^{18} cm^{-3} of Ag_2Se CQDs.

Keywords: Intraband transition; MIR detection; silver chalcogenide CQD.

DOI: https://doi.org/10.31349/RevMexFis.71.041304

1. Introduction

Currently, there is a rapidly expanding research focus on developing new optoelectronic devices that are opening the way to novel applications in detecting light in the mid-infrared (MIR) region. The mid-infrared region is of scientific interest in photodetection due to its alignment with atmospheric transparency windows. Moreover, it provides supplementary thermal information when contrasted with the visible or near-infrared regions [1]. The detection and sensing of MIR photons play an important role in applications such as remote sensing [2], defect inspection [3], medical diagnosis [4], environmental analysis [5], and material sensing and detection [6]. MIR photodetectors using HgCdTe, InSb, and other III-V superlattices demonstrate proper performance. However, the fabrication of these materials involves epitaxial growth on lattice-matched substrates through techniques such as molecular beam epitaxy or chemical vapor deposition, resulting in elevated costs. These high costs prevent the widespread application of MIR photodetectors in various fields due to the intricate material preparation and complex device fabrication processes [7, 8]. Therefore, there is a need for cost-effective materials to speed up their development and expand their applications [9]. In recent years, significant progress has been achieved in the field of sensitive MIR photodetectors, with special emphasis on the use of emerging materials such as graphene [10], black phosphorus [11], and colloidal quantum dots (CQDs) [12]. Colloidal quantum dots have attracted considerable attention as an alternative to conventional bulk epitaxial semiconductors, due to their distinct beneficial properties. These include the ability to tune the optical absorption wavelength based on size, facile solution processing, cost-effectiveness, and large-scale synthesis capabilities [13]. Self-doped CQDs, characterized by a tunable intraband absorption feature within the MIR spectrum through the integration of cost-effective synthesis and facile processing techniques, are a cost-effective alternative to conventional epitaxial MIR photodetectors [14, 15]. A significant advancement in the use of self-doped CQDs for MIR photodetection was characterized by the pioneering contributions of Guyot-Sionnest *et al*. They introduced the first mid-IR photodetector using intraband transition within HgSe CQDs [16]. Subsequently, based on this important achievement, Chen *et al*. significantly advanced the field by engineering an MIR photodetector with improved carrier mobility and precise doping modulation in HgSe CQDs [17]. Photodetectors relying on intraband transitions face challenges that require a critical examination of their limitations [18]. The pursuit of non-toxic infrared photodetectors appears as a promising frontier in this field [19]. Unfortunately, the predominant use of heavy metals, especially mercury, in most intraband transition materials raises concerns about their environmental effects, limiting their applications in biomedical fields due to inherent toxicity [20]. Due to this need, the use of non-toxic materials, such as Ag_2Se quantum dots, can potentially address such concerns. Consequently, it is important to investigate non-toxic MIR photodetectors with intraband transition to enhance their efficiency [21]. However, the current state of non-toxic Ag_2Se CQDs requires further investigation to refine their properties and optimize their suitability for MIR applications [22]. In their efforts to improve the responsivity of the photodetector, Shihab Bin Hafiz *et al*. introduced a novel approach by establishing a vertical heterojunction device comprising Ag_2Se-PbS CQD stacks. This innovative configuration not only restricted the dark current but also simplified the fabrication methods of the device [23]. Shihab Bin Hafiz *et al*. further optimized the structure using Ag_2Se CQDs and PbS CQDs. They reported a heterostructure device that was characterized by robust rectifier features. This combination promises to enhance the performance of photodetector devices comprised of Ag_2Se and PbS CQDs [24].

In the present study, we investigate a device characterized by a layered structure: Al/ZnO/Ag_2Se-PbS multi-barrier CQDs/Au. The active region of the photodetector employs Ag_2Se CQDs to induce intraband absorption, while PbS CQDs serve as a barrier material. Subsequently, we employ numerical simulations to compute the principal parameters of the photodetectors. Furthermore, we optimize the device performance by varying the size and doping density of the Ag_2Se CQDs and altering the number of layers of PbS CQDs within the barrier layer of the device.

2. Method and material

In this study, we employ a proposed structure, as depicted schematically in Fig. 1. The photodetector under investigation shares similarities with the device previously reported by Livache C. *et al*. [25] for toxic self-doped HgSe CQDs, which introduced a model for constructing a configuration capable of generating an electronic structure similar to that of a Multiple Quantum Well (MQW) structure with intraband absorption. However, this less toxic Ag_2Se-PbS structure used in this study differs in terms of the number of CQD layers within the barriers, as well as variations in CQD sizes and film doping densities.

The photodetector configuration comprises layers of Al/ZnO/Ag_2Se-PbS multi-barrier CQDs/Au. The bottom electrode is grid-shaped aluminum (Al), facilitating the transmission of mid-IR light. Within this configuration, ZnO nanoparticles serve as the hole-blocking layer (HBL) to effectively diminish dark current. Additionally, the active region comprises nine periods of self-doped Ag_2Se and PbS colloidal quantum dots (CQDs). The incorporation of Ag_2Se CQDs is important for realizing intraband absorption within the photodetector similar to the MQW structure (Fig. 2), while PbS CQDs function as a barrier layer in the structure. Finally, the Au layer is deposited as the bottom contact.

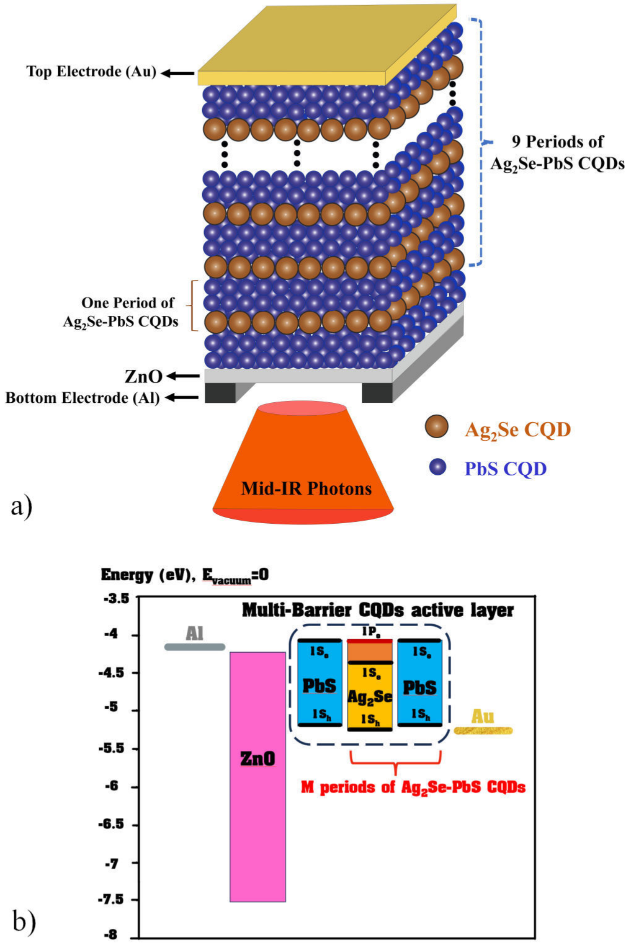

FIGURE 1. a) Schematic structure of the multi barrier CQD MIR photodetector. b) The energy level diagram of the materials used in the studied structure.

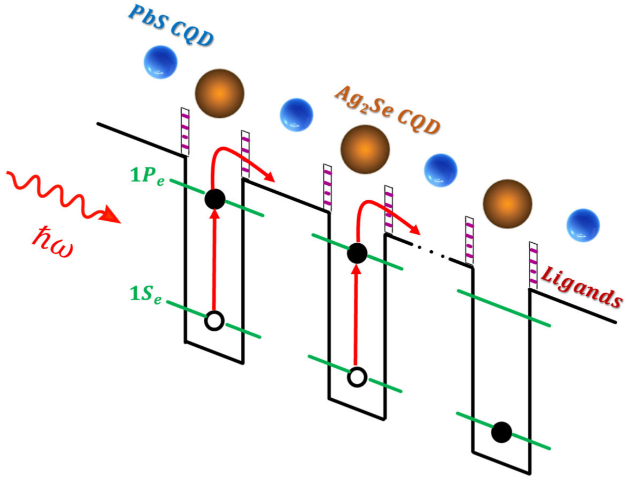

FIGURE 2. Schematic of structure of multi barrier CQD active region of photodetector, consisting of Ag_2Se CQDs as well and PbS CQDs as barrier.

To determine the performance parameters of the photodetector, it is necessary to perform a self-consistent numerical solution of both the Schrödinger and Poisson equations using the finite difference method. This procedure is essential for obtaining the eigenenergy, eigenfunction, electron concentrations corresponding to each energy level, and the potential profile within the Ag$_2$Se-PbS CQDs structure. The one-dimensional Schrödinger equation and the Poisson equation for the proposed structure are expressed as follows in Eq. (1) and (2) [26, 27]:

$$\left[-\frac{\hbar^2}{2}\frac{d}{dz}\left(\frac{1}{m_e^*}\frac{d}{dz}\right)+V(z)\right]\psi_n(z)=E_n\psi_n(z), \tag{1}$$

$$\frac{d}{dz}\left[\varepsilon(z)\frac{d}{dz}\right]\varphi(z)=-e\left(N_D(z)-n(z)\right), \tag{2}$$

where $\psi_n(z)$ is the wave function, E_n is the energy, V is the potential energy, $\hbar$ is Planck's constant divided by 2π , m_e^* is the electron effective mass, $\varepsilon(z)$ is the permittivity, e is the electron charge, $\varphi(z)$ is the electrostatic potential, $N_D(z)$ is the ionized donor concentration and n is the local density of confined electrons. $V(z)$ and $n(z)$ can be written as [28, 29]:

$$V(z)=\Delta E_{\text{BO}}-e\varphi(z), \tag{3}$$

$$n(z)=\frac{k_BTm_e^*}{\pi\hbar^2}\Sigma_n\ln\left[1+\exp\left(\frac{E_F-E_n}{k_BT}\right)\right]|\psi_n|^2. \tag{4}$$

Here, ΔE_{BO} is energy band offset, k_B is the Boltzmann constant, T is the temperature, E_n is the eigenenergy states and E_F is the Fermi level. In the simulation employing the Finite Difference Method, the proposed structure's inherent periodicity is accounted for by applying periodic boundary conditions to the wave functions. These conditions ensure spatial symmetry and impose continuity, described mathematically as $\psi_1=\psi_{n+1}$ and $\psi_0=\psi_n$. Furthermore, the Bias Voltage is designated as the reference potential at the boundaries of the simulated device domain, providing a consistent framework for solving the coupled Schrödinger and Poisson equations. In the subsequent investigation, the parameters acquired in the prior section are applied to derive performance parameters for the photodetector, including photocurrent, responsivity, dark current, and noise. Finally, utilizing these outcomes, the detectivity of the depicted structure in Fig. 1a) is determined. The photocurrent I_{photo} due to the absorption of MIR radiation in the device is given by [30]:

$$\begin{aligned}I_{\text{photo}}&=ev(F)n_0A_d\gamma^M\\&+\Bigg[eA_dI_0\exp\left(-\alpha(i-1)L_w\right)\left(1-\exp(-\alpha L_w)\right)\\&\times\frac{r_{\text{es},v}+r_{\text{es},th}}{r_{\text{es},v}+r_{\text{es},th}+r_r}\sum_{i=1}^{M}\gamma^{M-i}\Bigg],\end{aligned} \tag{5}$$

$$\gamma=\beta_c+(1-\beta_c)\frac{r_{\text{es},v}+r_{\text{es},th}}{r_{\text{es},v}+r_{\text{es},th}+r_r}, \tag{6}$$

where n_0 is electron density contribution, $(1-\beta_c)$ is capture probability at the interface of barrier-well, α is the intraband absorption coefficient, M is the number of periods of Ag_2Se CQDs, and I_0 stands for the intensity of light. $r_{\text{es},v}$, $r_{\text{es},th}$, and r_r define the escape rate due to external voltage, the escape rate due to temperature, and the rate of recombination, respectively, and α is the intraband absorption coefficient that is given by [31],

$$r_{\text{es},v}(V_b)=r_{es}(0)\exp\left[\frac{V_b}{V_{epl}}\right], \tag{7}$$

$$r_{\text{es},th}=\left(\frac{k_BT}{2\pi m_e^*L_w}\right)^{\frac{1}{2}}\exp\left[-\frac{V_{epl}}{k_BT}\right], \tag{8}$$

$$r_r=\frac{1}{\tau_r}, \tag{9}$$

$$\begin{aligned}\alpha&=\frac{e^2\omega n_{12}}{\varepsilon_0cn_{ref}}M_{21}(\cos\phi)^2,\\&\times\frac{\Gamma/2}{(E_2-E_1-\hbar\omega)^2+(\Gamma/2)^2},\end{aligned} \tag{10}$$

$$n_{12}=\frac{m^*k_BT}{\pi\hbar^2}\ln\left[\frac{1+\exp\left(\frac{E_F-E_1}{k_BT}\right)}{1+\exp\left(\frac{E_F-E_2}{k_BT}\right)}\right], \tag{11}$$

where $r_{\text{es}}(0)$ stands for the rate of emission of electrons under zero bias, V_{epl} stands for the effective potential barrier lowering that generally depends on the band offset, τ_r indicates carrier lifetime of electrons, ϕ is the incident angle of MIR photons, n_{12} is the effective density of electrons between two subbands, M_{21} is the dipole matrix element, Γ is the line width, and ω is the angular frequency of the MIR photons [30]. The concept of responsivity stands for quantifying the output electrical signal of the photodetector per input optical light. The responsivity $\Re$ can be expressed as [32]:

$$\Re=I_{\text{photo}}/P_{in}, \tag{12}$$

where, P_{in} is power of the incident IR light. The dark current, which can limit the sensitivity and performance of photodetectors, is modeled in the multi-barrier CQD MIR photodetector. The two dominant phenomena contributing to the dark current are the sequential resonant tunneling contribution and thermionic emission. Using Levine's model, the dark current can be expressed as [33]:

$$I_{dark}=I_{st}+I_{th}, \tag{13}$$

where I_{st} represents the contribution from sequential resonant tunneling and I_{th} represents the contribution from thermionic emission

$$I_{st}=\frac{eA_d}{\hbar {L_w}^2}T_{etp}(E,F)k_BT\ln \times\left[\frac{1+\exp\left(\frac{E_F}{k_BT}\right)}{1+\exp\left(\frac{E_F-eFL_b}{k_BT}\right)}\right], \tag{14}$$

$$I_{th}=\frac{em_e^*}{\pi\hbar^2}\frac{A_d\upsilon(F)}{L_w}eFL_b\exp\left[-\frac{E_B-eFL_w-E_F}{k_BT}\right], \tag{15}$$

where L_b and L_w are the barrier and well width, respectively, A_d is the detection area, F is the external electric field, E_B is the barrier height, m_b^* and m_e^* are the electron effective mass in the barrier and well, respectively. $\upsilon(F)$ is the effective drift velocity, and $T_{etp}(E,F)$ is the electron tunneling probability, given respectively by [34],

$$\upsilon(F)=\mu F/(1+(\mu F/\upsilon_s)^2)^{1/2}, \tag{16}$$

$$T_{etp}(E,F)=\exp\left(-\frac{4}{3\hbar eF}(2m_b^*)^{1/2}\times\left[\{E_B-eFL_w-E\}^{3/2}-\{E_B-eF(L_w+L_b)-E\}^{3/2}\right]\right), \tag{17}$$

where μ is the mobility and υ_s is the saturated velocity for electrons. The noise of IR photodetectors originates mainly from three sources, including shot noise, thermal noise, and flicker noise (significantly dominant at low frequencies and can be neglected here) [35]. The shot noise can be evaluated as [36]:

$$i_{\text{shot}}=[4e\,I_{\text{dark}}g_n\Delta f]^{1/2}. \tag{18}$$

The thermal noise can be expressed as [36]:

$$i_{\text{thermal}}=[4k_BT\Delta f/R_0]^{1/2}, \tag{19}$$

where g_n stands for the noise gain, Δf is the operating bandwidth of photodetector, and R_0 stands for the zero-bias resistance. The total noise current of photodetector can be evaluated as [36]:

$${i_{tn}}^2={i_{\text{shot}}}^2+{i_{\text{thermal}}}^2. \tag{20}$$

The detectivity is the most important performance parameter that characterizes the sensitivity and the general performance of IR photodetectors. The detectivity of the device can be defined as [37]:

$$D^*=\Re[A_d\Delta f]^{1/2}/i_{tn}. \tag{21}$$

3. Results and discussion

The Schrödinger and Poisson equations were discretized on uniform meshes using the finite difference method and iteratively solved until a self-consistent solution for electron concentrations at each level and the potential profile of Ag_2Se-PbS colloidal quantum dots was achieved. Subsequently, key performance parameters for the MIR CQD photodetector were determined based on the computed electron concentrations. To enhance the performance of the device, particularly in detecting weak input light and operating more effectively at elevated temperatures, a critical focus on optimizing the detectivity of CQD infrared photodetectors is essential. This optimization entails characterizing the dark current, photocurrent, responsivity, and noise properties through engineering of the device structure under varying temperature conditions. Figure 1 illustrates the configuration of a multi-barrier photodetector device. In this study, numerical calculations were employed to evaluate the performance parameters of a self-doped colloidal quantum dot mid-infrared photodetector at different temperatures. The primary objective was

TABLE I. Parameters for the multi-barrier Ag_2Se-PbS CQD photodetector [38–41]. m_0 is the free electron mass.

Parameter	Value
Ag_2Se CQDs diameter	3 to 6 nm
PbS CQDs diameter	5 nm
Film doping density of Ag_2Se CQDs	4×10^{18} to 10×10^{18} cm^{-3}
Ag_2Se CQDs fraction in active region	50%, 35%, 25%, 20%
Power of the incident MIR light (P_{in})	1 mW
Detection area of device (A_d)	200 × 200 μm
Electron mobility	19.4 cm^{2}V^{-1}s^{-1}
Dielectric constant of Ag_2Se (ε_r)	11
Dielectric constant of PbS (ε_r)	170
Ag_2Se effective electron mass (m_e^*)	0.32 m_0
PbS effective electron mass (m_b^*)	0.09 m_0

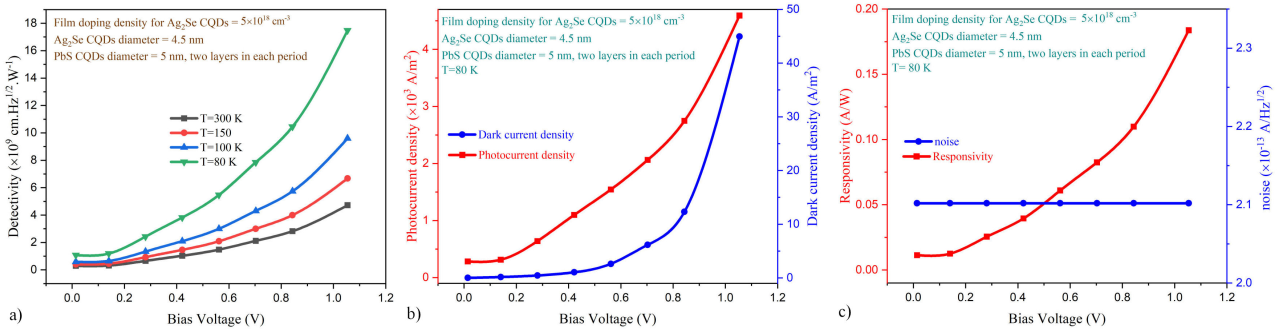

FIGURE 3. a) Detectivity of the device as a function of bias voltage, at different temperatures. b) Photocurrent density and Dark current density as a function of bias voltage, at $T = 80$ K. c) Responsivity and noise as a function of bias voltage, at $T = 80$ K, under MIR light illumination.

to enhance detectivity by optimizing the structural parameters of the device. Detectivity features were analyzed under diverse bias voltages, varied sizes, and film doping densities of colloidal quantum dots, along with changes in the number of PbS CQDs layers within the barriers at different temperatures. The incident mid-infrared photons were absorbed within the active region of a colloidal quantum dot MIR photodetector, resulting in the generation of photocarriers. This active region consisted of 9 periods of Ag$_2$Se-PbS CQD layers. It is assumed that within each layer (refer to Fig. 1), the Ag$_2$Se and PbS CQDs are uniformly distributed over a relatively large area, leading to a consistently spherical shape with an identical diameter. The key simulation parameters for the photodetector are summarized in Table I.

The colloidal quantum dots were passivated through the use of insulating long-chain ligands such as oleic acid (OA) or oleylamine. Subsequently, these ligands were replaced with conductive short-chain ligands such as ammonium thiocyanate (NH$_4$SCN). The process of exchanging ligands involved transferring the organic-capped CQDs to a polar solution, resulting in a significant improvement in mobility and enhanced photoresponse [42]. Changing from long-chain to short-chain (such as NH$_4$SCN) ligands led to a reduction in thickness. This reduction diminished barriers and increased carrier mobility. It is supposed that mobility remains relatively constant, regardless of particle size variations, as the study focuses on a narrow size range where mobility is near-optimal [43]. Figure 3a) illustrates the detectivity of the device as a function of bias voltage at various temperatures when exposed to MIR light. The quantum dots used in the study, Ag$_2$Se and PbS CQDs, have diameters of 4.5 nm and 5 nm, respectively. The film doping density for Ag$_2$Se CQDs is specified as 5×10^{18} cm^{-3}. Additionally, the active region comprises nine periods of Ag$_2$Se-PbS CQDs. The results depicted in Fig. 3 reveal an upward trend in detectivity with increasing bias voltage. This rise in detectivity is attributed to heightened photocurrent and responsivity. The trend observed in our study aligns with the findings reported in previous studies [44–46], exhibiting similar patterns in the dark current, photocurrent, and responsivity as functions of the bias voltage. On the other hand, the detectivity experiences a decline as the temperature rises. This phenomenon can be comprehended by considering various interconnected factors, including the escalation of thermal generation of carriers, an increase in dark current and carrier leakage, and a reduction in carrier lifetime.

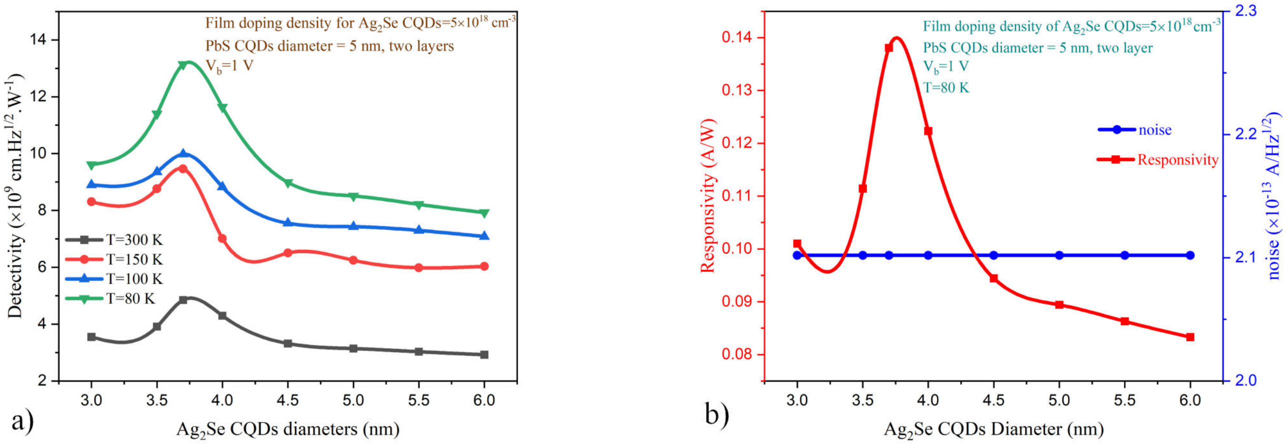

FIGURE 4. a) Detectivity of the device as a function of the diameter of Ag2Se CQDs, at different temperatures. b) Responsivity and total noise as a function of Ag$_2$Se CQDs film doping density, at $T = 80$ K.

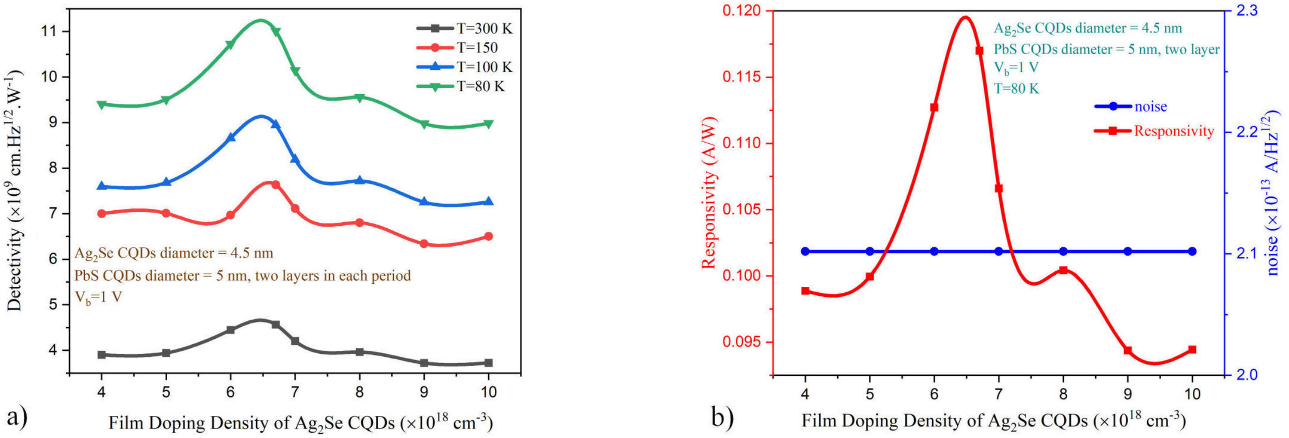

FIGURE 5. a) Detectivity of the device as a function of film doping density of Ag_2Se CQDs, at different temperatures. b) Thermal noise and dark-current shot noise as a function of film doping density of Ag_2Se CQDs, at $T = 80$ K. Responsivity and total noise as a function of film doping density of Ag_2Se CQDs, at $T = 80$ K.

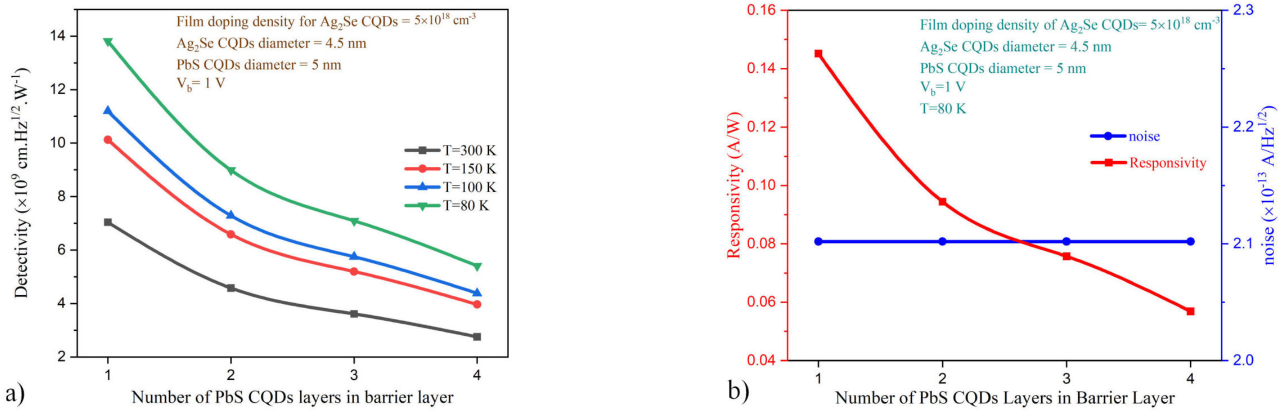

FIGURE 6. a) Detectivity of the device as a function of the different number of periods of the Ag_2Se-PbS CQDs in active region, at different temperatures. b) Responsivity and total noise as a function of the different number of PbS layers in barrier, at $T = 80$ K.

The first investigation of the device structure focuses on assessing how varying the diameter of Ag_2Se CQDs affects the detectivity of the photodetector. Figure 4 displays the variations in noise, responsivity, and detectivity in relation to the diameter of Ag_2Se CQDs, while maintaining constant film doping densities and a fixed diameter of PbS CQDs. The figure indicates that, at a constant temperature, an increase in the diameter of Ag_2Se CQDs initially enhances detectivity. This improvement is attributed to the heightened absorption associated with larger CQDs, resulting in increased responsivity. The variation between the absorption and the diameter of Ag_2Se CQDs follows a trajectory comparable to those observed in previous studies [47]. However, detectivity subsequently declines after reaching an optimal well width. This decline is attributable to amplified carrier trapping and non-radiative recombination processes, leading to a reduction in responsivity. Figure 4a) specifically depicts that the peak detectivity, reaching 13.13×10^9 Jones ($\mathrm{cm^2 Hz^{1/2} W^{-1}}$), occurs at 80 K for Ag_2Se CQDs with a diameter of 3.7 nm.

The next investigation aims to explore the impact of varying the doping density of Ag_2Se CQDs film on the detectivity of the MIR photodetector. Figure 5 depicts variations in noise, responsivity, and detectivity of the device concerning the film doping density of Ag_2Se CQDs, with a fixed applied bias, and CQD sizes.

The results indicate that, at a constant temperature, an increase in the film doping density of Ag_2Se CQDs initially boosts detectivity. This initial enhancement is attributed to the heightened electron concentration within the structure due to increased film doping density, resulting in an augmented photocurrent and improved responsivity of the photodetector, consequently leading to increased detectivity. However, as the film doping density of Ag_2Se CQDs continues to rise, various mechanisms, such as tunneling leakage current, come into play and can cause a decline in responsivity and detectivity beyond a certain threshold of film doping density. The optimal film doping density for achieving maximum detectivity is contingent upon multiple factors, including the specific design and material parameters of the photodetector. It is crucial to meticulously optimize the doping density to attain optimal performance in intraband photodetectors. Additionally, Fig. 5a) illustrates that the peak detectivity of 11.01×10^9 Jones ($\text{cmHz}^{1/2}\text{W}^{-1}$) was achieved at 80 K for a film doping density of 6.7×10^{18} cm^{-3} of Ag_2Se CQDs. This simulation reveals a pattern of change in the detectivity versus the film doping density consistent with previously published results [48]. In the final stage of investigation, we are exploring the impact of altering the number of layers of PbS CQDs within the barrier layer of the device on the detectivity of the MIR photodetector. Figure 6 presents the acquired data on noise, responsivity, and detectivity of the IR photodetector concerning the number of layers in the barrier for a constant film doping density of Ag_2Se CQDs and a fixed diameter of Ag_2Se and PbS CQDs.

Figure 6a) indicates a decline in the detectivity of the device as the number of layers containing PbS CQDs increases. This reduction in detectivity is attributed to various factors, including reduced carrier tunneling, increased carrier scattering, and shortened carrier lifetime, all contributing to a decrease in responsivity. The overall trend observed is a reduction in detectivity as the barrier width increases in the intraband MIR photodetector. The obtained results for the relationship between the detectivity and the number of layers of PbS CQDs within the barrier layer exhibit a trend consistent with previously reported findings [49].

4. Conclusion

To summarize, our investigation centered on the structure of a mid-infrared colloidal quantum dot photodetector composed of an Al/ZnO/Ag_2Se-PbS multi barrier CQDs/Au layer configuration, demonstrating intraband absorption. We explored how film doping density, the diameter of Ag_2Se CQDs, and the number of layers in the Ag_2Se-PbS CQDs films within the active region affect the photodetector's performance under a 1 V bias voltage. Our findings indicate that detectivity initially rises with the increasing diameter of Ag_2Se CQDs, leading to enhanced absorption and improved responsivity. However, beyond an optimal diameter, detectivity decreases due to increased carrier trapping and non-radiative recombination, causing a decline in responsivity. The peak detectivity of 13.13×10^9 Jones ($\text{cmHz}^{1/2}\text{W}^{-1}$) is observed at 80 K for Ag_2Se CQDs with an optimal 3.7 nm diameter. Increasing the film doping density of Ag_2Se CQDs initially enhances detectivity due to improved responsivity, but this improvement diminishes over time due to mechanisms like tunneling leakage current, resulting in decreased responsivity. The maximum detectivity, reaching 11.01×10^9 Jones (cm $\text{Hz}^{1/2}\text{W}^{-1}$), is achieved at 80 K with an optimal film doping density of 6.7×10^{18} cm^{-3} for Ag_2Se CQDs. Furthermore, the number of layers of PbS CQDs within the barrier layer impacts device detectivity. The detectivity of the device decreased with an increasing number of layers due to factors such as reduced carrier tunneling, increased carrier scattering, and reduced carrier lifetime, leading to a decrease in responsivity. In conclusion, our study provides insights into optimizing parameters for achieving peak detectivity in Ag_2Se-PbS CQD-based MIR photodetectors.

---

1. X. Xue *et al.*, High-operating-temperature mid-infrared photodetectors via quantum dot gradient homojunction. *Light Sci. Appl.*, **12.1** (2023) 2, `https://doi.org/10.1038/s41377-022-01014-0`
2. Y. Wang *et al.*, Mid-infrared single-pixel imaging at the single-photon level. *Nat. Commun.*, **14.1** (2023) 1073, `https://doi.org/10.1038/s41467-023-36815-3`
3. J. Fang *et al.*, Mid-infrared single-photon 3D imaging. *Light Sci. Appl.*, **12.1** (2023) 144, `https://doi.org/10.1038/s41377-023-01179-2`
4. H. Kumar and A. Kumar Pandey, GeSn-based multiple-quantum-well photodetectors for mid-infrared sensing applications. *IEEE Trans. Nanobiosci.*, **21.2** (2021) 175, `https://doi.org/10.1109/TNB.2021.3136571`
5. M. Hlavatsch and B. Mizaikoff, Advanced mid-infrared light-sources above and beyond lasers and their analytical utility. *Anal. Sci.*, **38.9** (2022) 1125, `https://doi.org/10.1007/s44211-022-00133-3`
6. S. Edelstein *et al.*, Waveguide-integrated mid-IR photodetector and all-optical modulator based on interlayer excitons absorption in a WS_2/HfS_2 heterostructure. *J. Nanophotonics*, **11.19** (2022) 4337, `https://doi.org/10.1515/nanoph-2022-0203`
7. Z. Liu *et al.*, Mid-Infrared HgTe Colloidal Quantum Dots In-Situ Passivated by Iodide. *Coatings*, **12.7** (2022) 1033, `https://doi.org/10.3390/coatings12071033`
8. S. B. Hafiz *et al.*, Silver selenide colloidal quantum dots for mid-wavelength infrared photodetection. *ACS Appl. Nano Mater.*, **2.3** (2019) 1631, `https://doi.org/10.1021/acsanm.9b00069`
9. M. Liu *et al.*, Colloidal quantum dot electronics. *Nat. Electron.*, **4.8** (2021) 548, `https://doi.org/10.1038/s41928-021-00632-7`
10. Q. Guo *et al.*, Efficient electrical detection of mid-infrared graphene plasmons at room temperature. *Nat. Mater.*, **17.11** (2018) 986, `https://doi.org/10.1038/s41563-018-0157-7`
11. J. Bullock *et al.*, Polarization-resolved black phosphorus/molybdenum disulfide mid-wave infrared photodiodes with high detectivity at room temperature. *Nat. Photonics*, **12.10** (2018) 601, `https://doi.org/10.1038/s41566-018-0239-8`
12. H. J. C. P. Zhang and P. Guyot-Sionnest, Intraband Transition of HgTe Nanocrystals for Long-Wave Infrared Detection at 12 μm. *ACS Nano*, **17.8** (2023) 7530, `https://doi.org/10.1021/acsnano.2c12636`
13. S. Zhang, Y. Hu, and Q. Hao, Advances of sensitive infrared detectors with HgTe colloidal quantum dots. *Coat-*

ings **10.8** (2020) 760, `https://doi.org/10.3390/coatings10080760`

14. B. Martinez *et al.*, HgSe self-doped nanocrystals as a platform to investigate the effects of vanishing confinement. *ACS Appl. Mater. Interfaces*, **9.41** (2017) 36173, `https://doi.org/10.1021/acsami.7b10665`
15. E. Lhuillier and P. Guyot-Sionnest, Recent progresses in mid infrared nanocrystal optoelectronics. *IEEE J. Sel. Top. Quantum Electron.*, **23.5** (2017) 1, `https://doi.org/10.1109/JSTQE.2017.2690838`
16. Z. Deng, K. S. Jeong, and P. Guyot-Sionnest, Colloidal quantum dots intraband photodetectors. *ACS Nano*, **8.11** (2014) 11707, `https://doi.org/10.1021/nn505092a`
17. M. Chen *et al.*, Mid-infrared intraband photodetector via high carrier mobility HgSe colloidal quantum dots. *ACS Nano*, **16.7** (2022) 11027, `https://doi.org/10.1021/acsnano.2c03631`
18. Q. Hao *et al.*, The Historical Development of Infrared Photodetection Based on Intraband Transitions. *Materials*, **16.4** (2023) 1562, `https://doi.org/10.3390/ma16041562`
19. H. Mølnȧs *et al.*, Understanding the Growth Mechanisms of Ultrasmall Silver Selenide Quantum Dots for Short-Wave Infrared Detectors. *Colloids Surf., A* **674** (2023) 131946, `https://doi.org/10.1016/j.colsurfa.2023.131946`
20. M. Shorie *et al.*, Graphitic carbon nitride QDs impregnated biocompatible agarose cartridge for removal of heavy metals from contaminated water samples. *J. Hazard. Mater.*, **367** (2019) 629, `https://doi.org/10.1016/j.jhazmat.2018.12.115`
21. J. Kim, D. Choi, and K. Seob Jeongm, Self-doped colloidal semiconductor nanocrystals with intraband transitions in steady state. *Chem. Commun.*, **54.61** (2018) 8435, `https://doi.org/10.1039/C8CC02488J`
22. M. M. A. Mahfuz *et al.*, Colloidal Ag_2Se intraband quantum dots. *Chem. Commun.* **59.72** (2023) 10722, `https://doi.org/10.1039/D3CC02203J`
23. S. B. Hafiz, M. M. Al Mahfuz and D.-K. Ko, Vertically stacked intraband quantum dot devices for mid-wavelength infrared photodetection. *ACS Appl. Mater. Interfaces*, **13.1** (2020) 937, `https://doi.org/10.1021/acsami.0c19450`
24. S. B. Hafiz *et al.*, Midwavelength infrared p-n heterojunction diodes based on intraband colloidal quantum dots. *ACS Appl. Mater. Interfaces*, **13.41** (2021) 49043, `https://doi.org/10.1021/acsami.1c14749`
25. C. Livache *et al.*, A colloidal quantum dot infrared photodetector and its use for intraband detection. *Nat. Commun.*, **10.1** (2019) 2125, `https://doi.org/10.1038/s41467-019-10170-8`
26. O. B. Boyraz, Self-consistent rate equation modeling of bi-functional quantum cascade structures. MS thesis. Middle East Technical University (2023).
27. K. S. Qwah *et al.*, Vertical hole transport through unipolar InGaN quantum wells and double heterostructures. *Phys. Rev. Mater.*, **6.4** (2022) 044602, `https://doi.org/10.1103/PhysRevMaterials.6.044602`
28. M. Moradi and M. Moradi, The Effects of Temperature and Electric Field on the Electronic and Optical Properties of an InAs Quantum Dot Placed at the Center of a GaAs Nanowire. *J. Surf. Invest.*, **16.6** (2022) 1237, `https://doi.org/10.1134/S1027451022060428`
29. A. Acharyya *et al.*, Self-consistent solution of Schrödinger–Poisson equations in a reverse biased nano-scale p-n junction based on Si/$Si_{0.4}Ge_{0.6}$/Si quantum well. *J. Comput. Electron.*, **14** (2015) 180, `https://doi.org/10.1007/s10825-014-0637-1`
30. M. A. Billaha, B. Roy, and N. Sahoo, Effect of external electric field on photo-responsivity of CdS/ZnSe multiple quantum well photodetector. *Superlattices Microstruct.* **157** (2021) 107003, `https://doi.org/10.1016/j.spmi.2021.107003`
31. M. A. Billaha, and M. K. Das, Performance analysis of AlGaAs/GaAs/InGaAs-based asymmetric long-wavelength QWIP. *Appl. Phys. A*, **125.7** (2019) 457, `https://doi.org/10.1007/s00339-019-2750-2`
32. K. Chen *et al.*, Two-In-One: End-Emitting Blue LED and Self-Powered UV Photodetector based on Single Trapezoidal PIN GaN Microwire for Ambient Light UV Monitoring and Feedback. *Small Methods*, **7** (2023) 2300138, `https://doi.org/10.1002/smtd.202300138`
33. B. F. Levine, Quantum-well infrared photodetectors. *J. Appl. Phys.*, **74.8** (1993) R1-R81, `https://doi.org/10.1063/1.354252`
34. E. M. I. N. E. Altin, M. Hostut, and Y. Ergun, Barrier lowering effect and dark current characteristics in asymmetric GaAs/AlGaAs multi-quantum well structure. *Appl. Phys. A*, **105** (2011) 833-839, `https://doi.org/10.1007/s00339-011-6634-3`
35. M. Khodaverdizadeh, and A. Asgari, Enhancing detectivity in mid-infrared photodetectors through structural parameter engineering in HgSe-HgTe colloidal quantum dots. *J. Nanophotonics*, **18.1** (2024) 016002-016002, `https://doi.org/10.1117/1.JNP.18.016002`
36. S. Wu *et al.*, High-performance back-illuminated $\mathrm{Ge}_{0.92}\mathrm{Sn}_{0.08}$/Ge multiple-quantum-well photodetector on Si platform for SWIR detection. *IEEE J. Sel. Top. Quantum Electron.*, **28.2** (2021) 1-9, `https://doi.org/10.1109/JSTQE.2021.3078894`
37. S. Madhusoodhanan *et al.*, High-temperature analysis of GaN-based MQW photodetector for optical galvanic isolations in high-density integrated power modules. *IEEE J. Emerging Sel. Top. Power Electron.* **9.4** (2020) 3877, `https://doi.org/10.1109/JESTPE.2020.2974788`.
38. V. González-Pedro *et al.*, High performance PbS Quantum Dot Sensitized Solar Cells exceeding 4 % efficiency: the role of metal precursors in the electron injection and charge separation. *Phys. Chem. Chem. Phys.*, **15.33** (2013) 13835-13843, `https://doi.org/10.1039/C3CP51651B`
39. O. Madelung, Semiconductors: data handbook, (Springer Science & Business Media, 2004)
40. M. Park *et al.*, Mid-infrared intraband transition of metal excess colloidal Ag_2Se nanocrystals. *ACS Photonics*, **5** (2018) 1907-1911, `https://doi.org/10.1021/acsphotonics.8b00291`

41. S. B. Hafiz *et al.*, Ligand engineering of mid-infrared Ag$_2$Se colloidal quantum dots. *Physica E*, **124** (2020) 114223, `https://doi.org/10.1016/j.physe.2020.114223`
42. P. Guyot-Sionnest, J. C. Peterson and C. Melnychuk, Extracting bulk-like semiconductor parameters from the characterization of colloidal quantum dot film photoconductors. *J. Phys. Chem. C*, **126** (2022) 17196, `https://doi.org/10.1021/acs.jpcc.2c05391`
43. M. Chen and P. Guyot-Sionnest, Reversible electrochemistry of mercury chalcogenide colloidal quantum dot films. *ACS Nano* **11** (2017) 4165, `https://doi.org/10.1021/acsnano.7b01014`
44. G. Biswal *et al.*, Bias-Tunable Quantum Well Infrared Photodetector. *J. Nanomater.*, **14** (2024) 548, `https://doi.org/10.3390/nano14060548`
45. F. Xie *et al.*, High-Performance InGaN/GaN Photodetectors With 30-Period Multiple Quantum Wells. *IEEE Trans. Electron Devices*, **70** (2023) 4685-4688, `https://doi.org/10.1109/TED.2023.3294348`
46. L. Guo *et al.*, Multiple-quantum-well-induced unipolar carrier transport multiplication in AlGaN solar-blind ultraviolet photodiode. *Photonics Res.*, **9** (2021) 1907-1915, `https://doi.org/10.1364/PRJ.435937`
47. N. Sfina, *et al.*, A multi-color $CdS/ZnSe$ quantum well photodetector for mid-and long-wavelength infrared detection. *Mater. Sci. Semicond. Process.* **19** (2014) 83-88, `https://doi.org/10.1016/j.mssp.2013.12.008`
48. M. A. Billaha, M. K. Das, and S. Kumar, Doping dependent frequency response of MQW infrared photodetector. *Superlattices Microstruct.* **104** (2017) 128-139, `https://doi.org/10.1016/j.spmi.2017.02.018`
49. S. D. Gunapala, and K. M. S. V. Bandara, Recent developments in quantum-well infrared photodetectors. *Thin Films*, **21** (1995) 113-237, `https://doi.org/10.1016/S1079-4050(06)80005-0`